PAPER

Check for updates

A ZnS–SnS₂/S–rGO ternary heterostructure for electrochemical detection of azo toxic dye sunset yellow in food samples†

Hanieh Ghaedi, Khadijeh Ghanbari iD * and Sepideh Bonyadi

High consumption of azo dyes such as sunset yellow (SY), widely used to improve the color and taste of some food products, is harmful and leads to diseases and problems in humans. Therefore, one of the important missions of scientists and researchers is to invent a fast and low-cost method to detect the amount of SY in food products. Here, we synthesized ZnS–SnS₂/S–rGO and modified a carbon paste electrode to design a sensor for SY determination in an aqueous environment and some real food samples. The morphology and structure of the ZnS–SnS₂/S–rGO were investigated by FE-SEM, HR-TEM, XPS, EDS, ATR-IR, Raman, and XRD techniques. Differentiated pulse voltammetry (DPV), cyclic voltammetry (CV), and electrochemical impedance spectroscopy (EIS) methods were used to study the electrochemical section. The designed sensor had a detection limit of 140 nM (S/N = 3) and a wide linear range of 3–100 μM and was used for SY determination in some real food samples with excellent recoveries (between 95.09 and 108.28%). This sensor has a high sensitivity and selectivity compared to the analog molecules with a similar structure for SY. It has commendable stability and satisfactory reproducibility.

1. Introduction

An essential category of food additives is synthetic colorants, which, due to their many advantages, such as being cheap, making the appearance of food more attractive, and their stable structure, are widely used in food production.[1] One of them is SY, where 2.5 mg kg⁻¹ bw⁻¹ day⁻¹ is the maximum allowed amount of daily consumption recommended by the EU.[2] Research indicates that overuse of SY might lead to several ailments, including bronchial asthma, attention deficit hyperactivity disorder, allergies, diarrhea, and dermal pruritus. Consequently, the amount of SY in food is controlled according to legal limits.[3] SY can be recognized by employing analytical techniques like enzyme-linked immunosorbent assay (ELISA),[4] capillary electrophoresis,[5] spectrophotometry,[6] HPLC-mass spectrometry,[7] high-performance liquid chromatography (HPLC) and thin-layer chromatography (TLC),[8] and electrochemical methods.[9,10] The electrochemical approach has attracted much interest in detecting SY because of its benefits, which include low cost, fast reaction, short detection procedure, and high sensitivity compared to other methods.[11]

To detect azo dyes, the electrochemical method employs electrochemical sensors featuring an optimal electrode characterized by a substantial surface area, superior electrical conductivity, commendable selectivity, and appropriate pore architecture.[12–14] Given that SY is an electroactive compound, the electrochemical approach is suitable for its identification. However, a challenge arises due to the presence of a mixture of food colorants, which regrettably interfere with the target food color (SY) signal on unmodified electrodes, compromising selectivity. Therefore, modification of the electrode surface is used to solve the abovementioned problem.[10]

Graphene, a prevalent material for electrode surface modification, consists of carbon atoms, resulting in highly stable chemical characteristics. Simultaneously, it can absorb and desorb several atoms and molecules, and its properties may be modified by doping. Among the drawbacks of graphene oxide-based electrodes, we can point out the low efficiency of initial colony power and reversible capacities, because its functional groups contain a lot of residual oxygen or large surface areas.[15] Doping is an efficacious way of solving such problems. Sulfur doping in graphene oxide sheets enhances electrochemical activity and electrical conductivity by creating exterior flaws and boosting specific capacitance *via* reversibility. Doping of heteroatoms like phosphorus, sulfur, and nitrogen is an effective method to influence the chemical and physical characteristics of carbon materials, including graphene, by altering electrical properties *via* defect creation and

Department of Analytical Chemistry, Faculty of Chemistry, Alzahra University, P. O. Box 1993891167, Tehran, Iran. E-mail: Kh.ghanbari@alzahra.ac.ir, Kh_ghanb@yahoo.com

resistance, as well as enhancing interlayer spacing. A group of scientists showed that sulfur doping can increase the distance between layers of carbon materials.[16] Graphene oxide is known as one of the most stable chemical materials, but it suffers from the restacking of functional groups created in its synthesis, which can be solved by doping heteroatoms. Sulfur doping in graphene oxide sheets can increase electrochemical activity and electrical conductivity by increasing the effective surface area. Fortunately, the inherent properties of graphene oxide, such as the distance between layers and its resistance, allow oxygen-containing groups on graphene oxide to be replaced by sulfur atoms that have similar chemical properties.[17,18]

Recently, transition metal sulfides (TMS) such as SnS_2, MoS_2, WS_2, and CeS, along with their composites, have attracted considerable attention due to their unique band gap, exceptional catalytic properties, and high electrical conductivity. Tin(IV) is not categorized as a transition metal; yet, tin disulfide (SnS_2) possesses a crystalline structure similar to that of CdI_2-type transition metal sulfides, distinguished by layers of Sn atoms interspersed between two layers of closely packed S atoms, held together by weak van der Waals interactions.[19] Because of its low toxicity, affordability, and durability in non-alkaline environments, tin disulfide (SnS_2), an n-type semiconductor with a visible optical band gap of 2.2 eV, has garnered much interest.[20] However, its electron–hole performance is inadequate due to the fast recombination of electron–hole pairs, restricting its direct use; graphene might improve electron transport and hence boost the performance of SnS_2.[21,22]

Scientists are interested in zinc sulfide (ZnS), a very promising metal chalcogenide, because of its inherent properties, which encompass superior electrical mobility, water insolubility, thermal stability, cost-effectiveness, and non-toxicity. ZnS is an n-type semiconductor photocatalyst that demonstrates significant chemical stability against hydrolysis and oxidation, along with a negative oxidation potential. ZnS appears in several morphologies, including cubic (sphalerite) and wurtzite, in a tetrahedral framework. Semiconductor materials like ZnS exhibit physical and chemical stability and a substantial band gap.[23,24]

However, single TMSs have limitations such as slow ion transport kinetics and poor electrical conductivity, which limit their applications. Therefore, rational designs in the composition and structure of these compounds can overcome these limitations. In particular, bimetallic sulfides, consisting of two metallic elements (Co, Fe, Sn, Zn, etc.), have higher catalytic activity, mechanical stability, and electrical conductivity due to their abundant redox sites and possible synergistic effects.[25,26] Liu and co-workers synthesized the bimetallic sulfide H-$Zn_{0.3}$-$Co_{2.7}S_4$ by facile co-precipitation and solvothermal sulfidation methods and used it to design an electrochemical sensor for dopamine measurement.[27] Disouza and colleagues synthesized the $ZnS:SnS_2@EGO$ nanocomposite by a hydrothermal method and used it for electrochemical measurement of the carcinogenic pollutant maleic hydrazide.[28] Li and colleagues synthesized the $MoO_3/ZnCdS$ nanocomposite and used it for the simultaneous measurement of 4-nitrophenol and Cr(VI) using a photoelectrochemical sensor. The designed sensor showed

very good stability, reproducibility, and selectivity, and was used to measure these compounds in real samples.[29]

Heterogeneous structures containing different compounds can facilitate the reaction kinetics and increase the electron transfer rate. Considering the advantages and disadvantages of each of the mentioned materials, we turned to the synthesis of sulfur-doped graphene oxide (S–rGO) and the heterogeneous structure of $ZnS–SnS_2$ with easy conversion of precursors through the hydrothermal method, which is an easy and highly efficient method.[30] The $ZnS–SnS_2$ microcubes were synthesized by direct conversion of the cubic precursor $ZnSn(OH)_6$, and for the first time, the $ZnS–SnS_2/S–rGO$ nanocomposite was prepared by dispersing sulfide microcubes ($ZnS–SnS_2$) on S–rGO nanosheets. Due to the extraordinary capabilities of the S–rGO nanostructure, the combination of bimetallic sulfide with S–rGO resulted in a nanocomposite that was used in the design of a modified electrochemical sensor for the determination of SY. Due to the improved performance and efficiency, and the beneficial properties of this nanocomposite, the proposed sensor showed excellent performance for the detection of SY in some food samples.

2. Experimental section

2.1. Chemicals and instruments

All materials used in this study were purchased from Merck and were analytical reagent grade, including: graphite powder, nujol oil, potassium chloride, hydrochloric acid, sodium hydroxide, potassium ferrocyanide, acetic acid, sulfuric acid, zinc chloride, tin(IV) chloride, sodium hydroxide, sunset yellow, tartrazine, potassium permanganate, hydrogen peroxide, sodium nitrate, sodium sulfide, ethanol, citric acid, and thioacetamide. The phosphate buffer solution (PBS, 0.1 M, pH = 7.5) was used as a supporting electrolyte. All solution preparation was done using double-distilled water. The used instruments were as follows: a Metrohm Autolab B. V.® Autolab PGSTAT 101 potentiostat/galvanostat (Utrecht, UT, the Netherlands) (including a three-electrode cell system, a bare or modified carbon paste electrode (CPE) as a working electrode, an Ag/AgCl/saturated KCl as a reference electrode, and a platinum wire as a counter electrode) for electrochemical section determinations, a field emission scanning electron microscope (FE-SEM) with an accelerating voltage of 20 kV (MIRA 3, TESCAN, Czech Republic) and a Philips EM208S 100 kV high-resolution transmission electron microscope (HRTEM) for morphology investigation, X-ray diffraction (XRD) with an X'Pert MPD (Philips, Netherlands), a UV-vis spectrophotometer (UV-2600, Shimadzu, Japan) for DRS spectra recording, and a Tensor 27 (Bruker) with KBr pellets for IR spectra recording.

2.2. Synthesis of cubic-like $ZnSn(OH)_6$

Initially, 4 mmol of $SnCl_4$ was dissolved in 20 mL of ethanol. The solution was added to a mixture comprising 4 mmol of citric acid and 4 mmol of $ZnCl_2$ in 140 mL of deionized water. Subsequently, 20 ml of 2 M NaOH solution was incrementally added to the preceding solution, which was undergoing vigorous agitation. After 60 minutes, an extra 60 ml of NaOH

solution was added all at once, leading to the emergence of a white precipitate after 30 minutes. The resulting product underwent multiple centrifugation cycles with ethanol and deionized water, and was thereafter dried in an oven at 60 °C, and was identified as ZnSn(OH)$_6$.[31]

2.3. Preparation of ZnS–SnS$_2$

To produce ZnS–SnS$_2$, 5 mL of acetic acid was slowly introduced to a solution containing 3 g of precipitate (ZnSn(OH)$_6$) and 5 mmol of thioacetamide in 25 mL of deionized water while continuously stirring. The obtained solution was transferred to an autoclave and subjected to an oven temperature of 160 °C for 10 hours, yielding a yellow precipitate. The resulting solution was subjected to centrifugation with deionized water and ethanol many times, and thereafter it was dried at 60 °C in an oven, and designated as ZnS–SnS$_2$.[31]

2.4. Preparation of S–rGO

Graphene oxide was initially manufactured by the modified Hummers process, and for sulfur doping, 3 mg of graphene oxide was distributed in 5 mL of deionized water. After this step, 1 mL of 0.5 M Na$_2$S solution was included and subjected to sonication for 15 minutes. A further 15 minutes was conducted in a 100 °C water bath. The procedure was reiterated, and the resultant precipitate was subjected to centrifugation with deionized water many times, thereafter it was dried at 60 °C in an oven, and designated as S–rGO.[32]

2.5. Preparation of ZnS–SnS$_2$/S–rGO

To do this, 0.12 g of S–rGO was dispersed in 40 mL of deionized water, whereas 0.24 g of ZnS–SnS$_2$ was distributed in 3 mL of deionized water, with both solutions sonicated separately for 15 minutes. The two scattered solutions were thereafter combined and stirred for 10 minutes. Subsequently, it was placed into an autoclave at 170 °C for 4 hours. The resulting precipitate was subjected to centrifugation with ethanol and deionized water many times, and thereafter dried at 80 °C in an oven, and designated as ZnS–SnS$_2$/S–rGO.[30]

2.6. Fabrication of the sensor

To make a uniformly consistent paste, 70% graphite powder and 30% nujol oil were initially combined manually for 15 to 30 minutes. A copper wire was then put into the cut insulin syringe (d = 3.5 mm) to establish electrical contact with the electrode after this homogeneous mixture had been fully compressed. In this way, a bare CPE is ready.[33] For the preparation of the modified CPE, namely ZnS–SnS$_2$/S–rGO/CPE, it was done in this way: 0.08 g ZnS–SnS$_2$/S–rGO was dispersed in 2 mL ethanol for 10 min, and then 60 μL of it was dropped on the bare CPE surface and allowed to dry to be ready for use. A schematic of these steps is presented briefly in Scheme 1.

3. Results and discussion

3.1. Characterization of ZnS–SnS$_2$/S–rGO/CPE

FE-SEM images of ZnSn(OH)$_6$ with different magnifications are demonstrated in Fig. 1(a and b). According to this figure, the
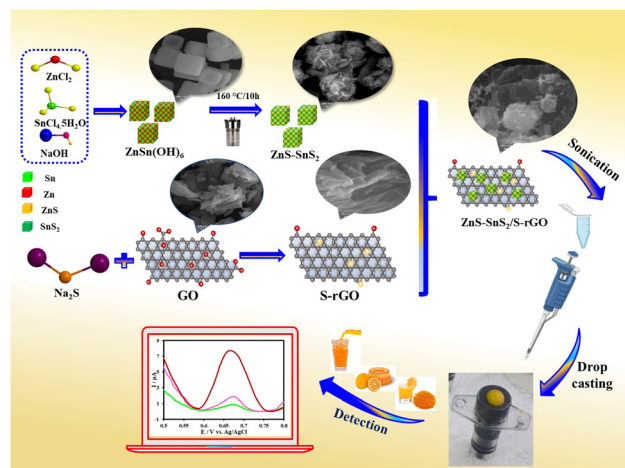
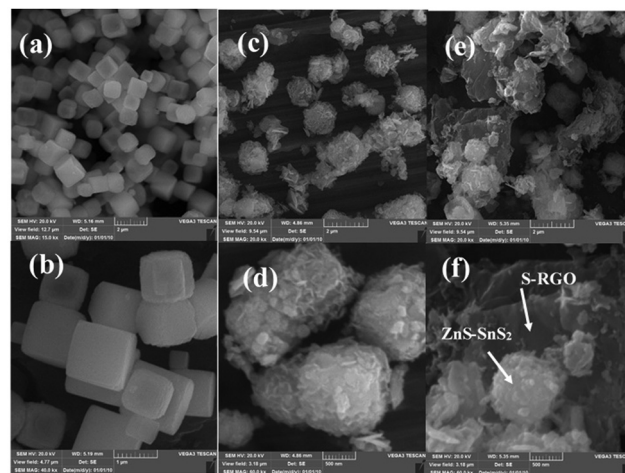Scheme 1 Schematic illustration of ZnS–SnS$_2$/S–rGO/CPE preparation for SY determination.

Fig. 1 FE-SEM images of (a) and (b) ZnSn(OH)$_6$ precursor, (c) and (d) ZnS–SnS$_2$, and (e) and (f) ZnS–SnS$_2$/S–rGO.

ZnSn(OH)$_6$ precursor has high monodispersity and a homogeneous cube architecture. These microcubes have an average diameter of around 2 μm. The ZnS–SnS$_2$ sample is shown in Fig. 1(c and d) as microcubes that are packed with stacks of two-dimensional ultrathin nanoparticles and a few small nanoparticles, and have an average size of 1.7–2.0 μm. Fig. 1(e and f) shows the SEM image of the ZnS–SnS$_2$/S–rGO composites at different magnifications, and it can be seen that ZnS–SnS$_2$ microcubes are present along with S–rGO ultrathin sheets. Charges and ion transport may be efficiently improved by conductive and flexible S–rGO nanosheets.

Fig. S1a–c (ESI†) shows the EDX spectrum of ZnSn(OH)$_6$, ZnS–SnS$_2$, and ZnS–SnS$_2$/S–rGO, respectively. In Fig. S1a (ESI†), the presence of O, Sn, and Zn elements; and in Fig. S1b (ESI†), S, Zn, and Sn elements; proved the successful synthesis of ZnSn(OH)$_6$ and ZnS–SnS$_2$, respectively. Fig. S1c (ESI†) demonstrates the effective synthesis of the ZnS–SnS$_2$/S–rGO nanocomposite, as evidenced by the presence of all constituent elements: Zn, Sn, C, O, and S.
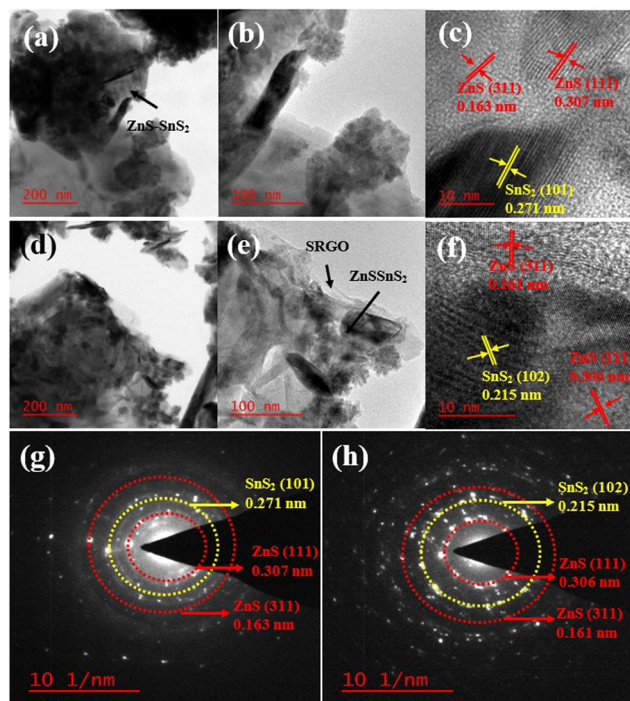
Fig. 2 (a) and (b) Low and high magnification TEM of ZnS–SnS$_2$, (c) HR-TEM micrograph of ZnS–SnS$_2$, (d) and (e) low and high magnification TEM of ZnS–SnS$_2$/S–rGO, (f) HR-TEM micrograph of ZnS–SnS$_2$/S–rGO, and (g) and (h) SAED pattern of ZnS–SnS$_2$ and ZnS–SnS$_2$/S–rGO, respectively.

Fig. 3 XRD patterns of GO, S–rGO, ZnSn(OH)$_6$, ZnS–SnS$_2$, and ZnS–SnS$_2$/S–rGO.

The internal structure and morphology of the ZnS–SnS$_2$ and ZnS–SnS$_2$/S–rGO nanocomposites were examined using selected area electron diffraction (SAED) patterns, high-resolution TEM (HR-TEM), and conventional transmission electron microscopy (TEM). Comprehensive HR-TEM and TEM images of ZnS–SnS$_2$ are shown in Fig. 2(a–c). A high magnification TEM picture (Fig. 2b) confirms the micro cube structure with a thin brim seen in Fig. 2a. A considerable region of the black shadow suggests that this nanocomposite is composed of nanoplates and nanoparticles, which is consistent with the SEM morphology. The embedding of nanoparticles in S–rGO is confirmed by typical TEM images of the nanocomposite ZnS–SnS$_2$/S–rGO (Fig. 2d and e)). Fig. 2c and f shows lattice-resolved HR-TEM images of the ZnS–SnS$_2$ and ZnS–SnS$_2$/S–rGO nanocomposites, respectively. According to Fig. 2(c and f), the interplanar spacings of 0.163 and 0.161 nm correspond well with the (311) plane of ZnS, and the d-spacings 0.307 and 0.306 nm correspond to the (111) plane of ZnS (PDF# 77-2100), while the d-spacings of 0.271 and 0.215 nm correspond to the (101) and (102) planes of SnS$_2$, respectively (PDF# 23-0677). The HR-TEM data show good agreement with the XRD and SEM results. A set of distinct diffraction rings is produced using SAED patterns (Fig. 2(g and h)). These rings are completely indexed to the (111) and (311) planes of ZnS and the (101) and (102) planes of SnS$_2$, respectively.[31,34,35]

The materials' crystalline phase and grain size were described using powder X-ray diffraction (XRD) measurement. The XRD patterns of the ZnSn(OH)$_6$, ZnS–SnS$_2$, S–rGO, pure GO, and ZnS–SnS$_2$/S–rGO nanocomposite are shown in Fig. 3. The XRD
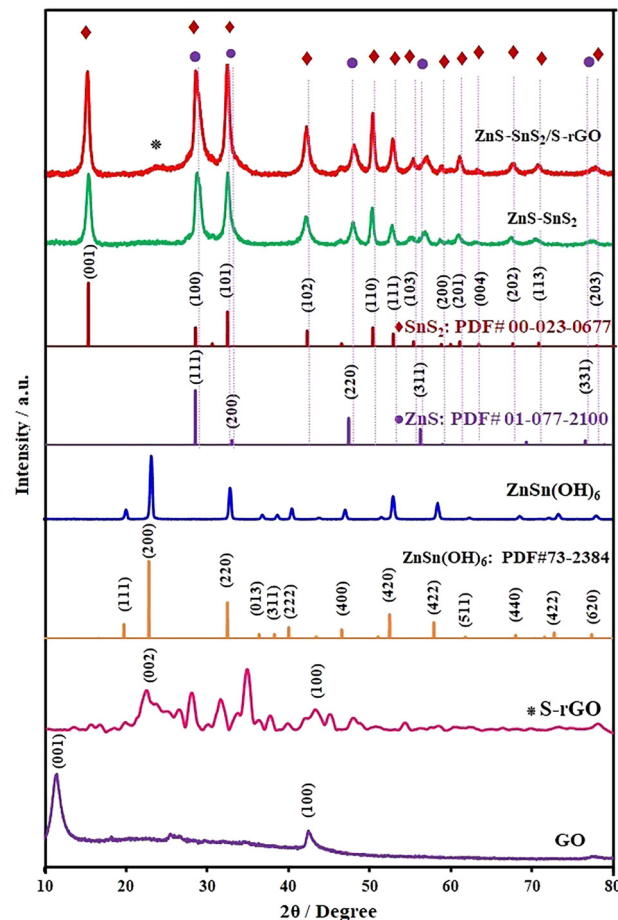
pattern of GO displays the characteristic (001) plane at $2\theta =$ 11.5° with a distance of 0.77 nm, signifying the presence of oxygenated functional groups such as carboxyl, epoxy, and carbonyl. The peak at $2\theta = 41.57$° represents the carbon's hexagonal structure.[36,37] Fig. 3 illustrates that the XRD pattern of S–rGO displays a broad peak for graphene planes in the $2\theta =$ 23° area, attributed to reduced oxygenated groups and the decreased interplanar distance (0.40 nm) between the (002) planes. This finding confirms the reduction of graphite oxide, as evidenced by the removal of the pronounced peak in the 11.5° area.[38,39] Fig. 3 illustrates that the XRD pattern of the produced ZnSn(OH)$_6$ microspheres displays specific diffraction peaks corresponding to the cubic phase of ZnSn(OH)$_6$ (JCPDS No. 73-2384). The distinct peaks, devoid of any extraneous peaks, signify the great purity and exceptional crystallinity of the precursor.

The XRD patterns of the ZnS–SnS$_2$/S–rGO nanocomposite closely align with those of the pristine ZnS–SnS$_2$ sample, exhibiting 2θ values of 28.5°, 33.1°, 47.4°, 56.3°, and 76.0°, which correspond to the (111), (200), (220), (311) and (331) crystal planes of cubic ZnS, respectively (PDF# 01-077-2100). The peaks at 2θ values of 15.0°, 28.2°, 32.1°, 41.9°, 49.9°, 52.4°, 54.9°, 60.6°, and 70.3°, correspond to the (001), (100), (101),
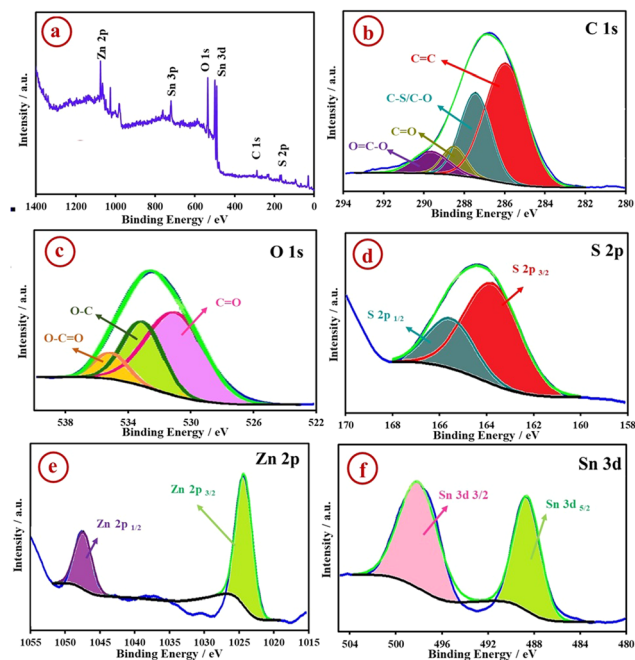
Fig. 4 The XPS (a) survey spectrum, (b) C 1s, (c) O 1s, (d) S 2p, (e) Zn 2p, and (f) Sn 3d high-resolution XPS spectra of the ZnS−SnS$_2$/S−rGO.

(102), (110), (111), (103), (201), and (113) crystal planes of SnS$_2$, respectively (PDF# 00-023-0677). On the other hand, the XRD spectrum of the ZnS−SnS$_2$/S−rGO nanocomposite peaks at about 23°, mainly due to the presence of S−rGO.[31] The strong XRD peaks denote orthorhombic SnS$_2$ and cubic ZnS structures, signifying enhanced crystallinity and grain growth.[40–42] The nanocomposite pattern exhibits distinct peaks corresponding to ZnS−SnS$_2$ and S−rGO, therefore confirming the effective synthesis of the ZnS−SnS$_2$/S−rGO nanocomposite.

The sample was then analyzed using X-ray photoelectron spectroscopy (XPS) to look into the elemental status and chemical composition of each species. Fig. 4a shows the full XPS spectrum of ZnS−SnS$_2$/S−rGO, further illustrating the co-existence of Zn, Sn, C, O, and S elements. In the XPS spectrum of C 1s (Fig. 4b), four main peaks with the binding energies at 285.94 eV, 287.44 eV, 288.53 eV, and 289.69 eV are assigned to C=C, C–S/C–O, C=O, and O=C–O bonds, respectively.[43] As presented in Fig. 4c, the high-resolution O 1s spectrum can be fitted into three peaks at 532.97 eV, 534.16 eV, and 535.30 eV, which are assigned to the C=O, O–C, and O–C=O, respectively.[44] As exhibited in Fig. 4d, the high-resolution spectrum of S 2p, is separated into S 2p$^{3/2}$ and S 2p$^{1/2}$ at 163.69 eV and 165.49 eV, respectively.[45] The high-resolution spectrum of Zn 2p (Fig. 4e) shows peaks of Zn 2p$^{1/2}$ and Zn 2p$^{3/2}$ at 1046.95 eV and 1023.85 eV, respectively. The distance between these Zn 2p peak positions is 23.1 eV, which can be attributed to the state of Zn^{2+} and agrees well with previous reports.[46,47] In the high-resolution XPS spectrum of Sn 3d (Fig. 4f), Sn 3d$^{3/2}$ and Sn 3d$^{5/2}$ peaks are detected with binding energies at 498.06 eV and 488.58 eV, respectively.[48]

FTIR spectra of GO, S−rGO, ZnS−SnS$_2$, and ZnS−SnS$_2$/S−rGO were recorded and the obtained results are shown in Fig. 5. The FTIR spectra of the pristine GO sheets reveal the presence of several functional groups, including C=O stretching from the carbonyl, broad –OH stretching, and carboxyl vibrations, and C=C skeletal stretching vibrations at 1713, 3418, and 1621 cm^{-1}, respectively. Also C–O stretching peaks of alkoxy and epoxy at 1049 cm^{-1} and 1225 cm^{-1} were observed.[49] Also, when comparing S−rGO to GO, the relative intensities of –OH, C=O, C–OH, and C–O become weak or almost nonexistent, showing that the oxygen-containing groups are massively eliminated during the reduction treatment.[50,51] For the S−rGO spectrum, the peak at 1123 cm^{-1} corresponds to the vibrations of C–S–C.[52,53] In the S−rGO spectrum, the C–O–C bonding signal was not present; this result indicates that the epoxide group of GO converted into C–S–C or C–S. Moreover, the pronounced absorption bands between 500–660 cm^{-1} for ZnS−SnS$_2$ and ZnS−SnS$_2$/S−rGO were associated with the vibrational characteristics of Zn–S and Sn–S. The resonance interaction among the vibrational modes of sulfide ions within the crystal lattice was proved by group peaks near 1000 cm^{-1}.[54,55]

Because Raman spectroscopy is highly sensitive to the electrical structure, degree of hybridization, crystal disorder, and quantity of chemical changes of carbon nanostructures, it may be used to gain important information about graphene and its derivatives. Fig. 6 shows the Raman spectra of GO, S−rGO, ZnS−SnS$_2$, and ZnS−SnS$_2$/S−rGO. The four characteristic peaks in the spectrum are the D, G, 2D, and D + G peaks. The D and G bands were found at 1348 and 1594 cm^{-1} in pristine GO, respectively. While the G band originates from the vibrations of sp^2 carbon atoms in graphitic hexagonal lattices, the D band is associated with the vibrations of sp^3 carbon atoms associated with defects and disorder.[56,57] Moreover, the D + G peak is a combined scattering peak, and the 2D peak represents the second-order disorder mode due to an alternate in-plane
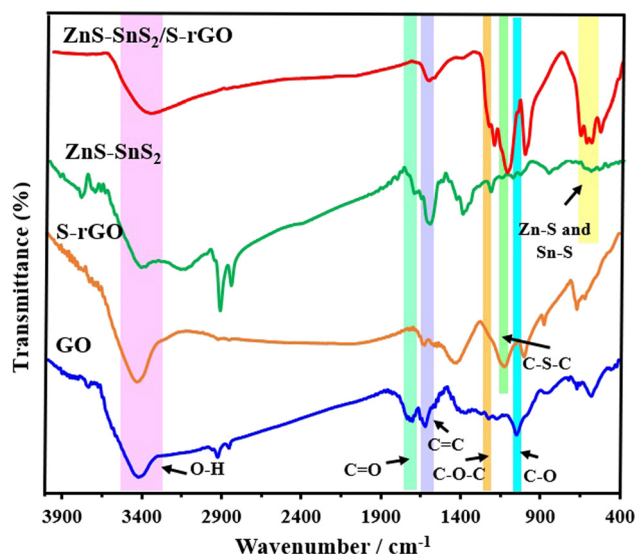

Fig. 5 FT-IR of GO, S−rGO, ZnS−SnS$_2$, and ZnS−SnS$_2$/S−rGO.
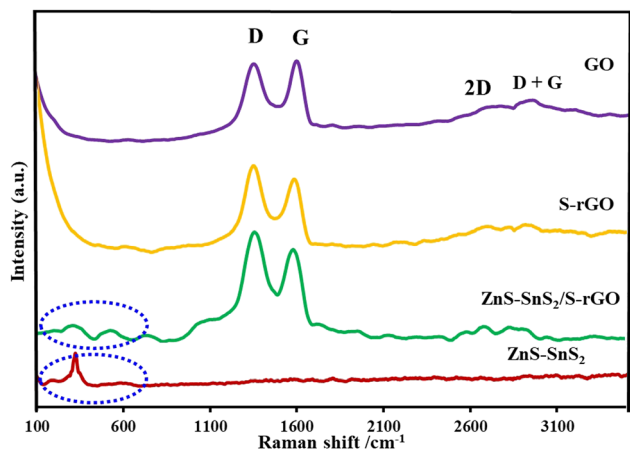
Fig. 6 Raman spectra of GO, S–rGO, ZnS–SnS$_2$, and ZnS–SnS$_2$/S–rGO.

vibration.[56] All of the peaks in S–rGO showed a minor redshift (leftward shift), with the D and G bands showing up at 1343 and 1579 cm^{-1}, respectively. This was explained by structural reordering that occurred during the reduction and sulfonation process. In S–rGO, the intensity of the D band was higher than that of the G band, signifying a structural degradation of the sp^2 carbon lattice due to the reduction of oxygen functions in graphene oxide; moreover, the induced sulfur ions promote further disorder. The D band of the ZnS–SnS$_2$/S–rGO nanocomposites, beside GO, exhibited a blue shift at 1351 cm^{-1}, whereas the G band had a little red shift at 1578 cm^{-1}. These shifts in the Raman spectra suggest the presence of interactions between ZnS–SnS$_2$ and GO.[58,59] The intensity ratio of the D and G bands (I_D/I_G) for GO, S–rGO, and ZnS–SnS$_2$/S–rGO is 0.99, 1.21, and 1.22, respectively.[60] The results show that the oxygen functions of GO have been partly decreased, and sulfur ions have been incorporated into the carbon lattices.[61] The Raman spectra for ZnS–SnS$_2$ and ZnS–SnS$_2$/S–rGO display additional bands indicative of the presence of ZnS–SnS$_2$ in the composite material.[62,63] Hence proving the coexistence of both components in the hybrid structure.

3.2. Electrochemistry of ZnS–SnS$_2$/S–rGO/CPE

The electrochemical properties of ZnS–SnS$_2$/S–rGO/CPE were measured using the redox probe. For this purpose and electroactive surface area determination, CVs were recorded in 1 mM [Fe(CN)$_6$]$^{3-/4-}$ in 0.1 M KCl solution in the scan rate range of 10–100 mV s^{-1} for the bare CPE, ZnS–SnS$_2$/CPE, S–rGO/CPE, and ZnS–SnS$_2$/S–rGO/CPE and are shown in Fig. S2(a–d) (ESI†), respectively. The calculation employed the Randles–Sevcik eqn (1):[45]

$$I_p = (2.69 \times 105)n^{3/2}ACD^{1/2}v^{1/2} \tag{1}$$

I_p denotes the peak current, D represents the diffusion coefficient of [Fe(CN)$_6$]$^{3-/4-}$ (6.2 × 10^{-6} cm^2 s^{-1}), A indicates the electroactive area (cm^2), n signifies the number of electrons, v refers to the scan rate (V s^{-1}), and C is the concentration of [Fe(CN)$_6$]$^{3-/4-}$ (M). The electroactive surface areas were

calculated to be 0.21, 0.03, 0.35, and 1.33 cm^2 for the bare CPE, ZnS–SnS$_2$/CPE, S–rGO/CPE, and ZnS–SnS$_2$/S–rGO/CPE, respectively. The surface area obtained with the ZnS–SnS$_2$/S–rGO/CPE was 6.33-fold higher than the value for the CPE. The findings demonstrated that the incorporation of ZnS–SnS$_2$ and S–rGO enhanced the electroactive surface area of the electrode, hence augmenting the peak current intensity.[64]

To evaluate the electrochemical activity of the bare CPE, ZnS–SnS$_2$/CPE, and ZnS–SnS$_2$/S–rGO/CPE, both electrochemical impedance spectra (EIS) and CV results are presented. Fig. 7a illustrates the CV curves of the bare and modified CPE in a 0.1 M KCl solution containing 1 mM [Fe(CN)$_6$]$^{3-/4-}$ at a scan rate of 100 mV s^{-1}. The peak potential difference (ΔE_p) for the bare CPE, ZnS–SnS$_2$/CPE, and ZnS–SnS$_2$/S–rGO/CPE were measured at 0.48 V, 0.41 V, and 0.11 V, respectively. Modifying the CPE surface with ZnS–SnS$_2$/S–rGO enhanced the redox peak current and reduced the peak potential difference (ΔE_p). The anodic peak current of ZnS–SnS$_2$/S–rGO/CPE was almost 6.11 times greater than that of the bare CPE. The high redox peak current of the ZnS–SnS$_2$/S–rGO/CPE nanocomposite can be attributed to its substantial specific surface area, the enhanced number of active sites by sulfur-doped RGO, and quick electron transfer; these characteristics indicate that the ZnS–SnS$_2$/S–rGO nanocomposite possesses unique electrocatalytic activity.

The interfacial electron transport properties of several modified electrodes were examined by electrochemical impedance spectroscopy (EIS). Fig. 7(b and c) shows the Nyquist plots of electrochemical impedance spectra of the bare CPE, ZnS–SnS$_2$, and ZnS–SnS$_2$/S–rGO modified CPE in 1 mM [Fe(CN)$_6$]$^{3-/4-}$ containing 0.1 M KCl under 0.15 V. As shown in Fig. S3 (ESI†), the EIS curves obtained from the experiment were examined by fitting them to the standard Randle's equivalent circuit. The impedance data of the bare GCE and other modified GCEs had two components. One segment is linear, while the other is semi-circular; the linear segment is associated with the

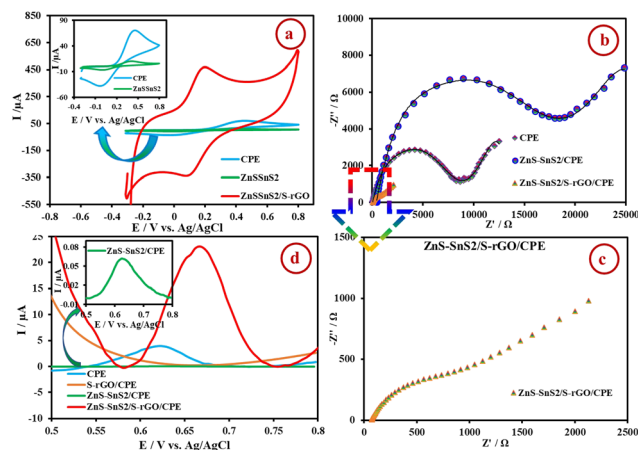**Fig. 7** (a) CVs, (b) and (c) Nyquist plots from 10^5 Hz to 10^{-1} Hz frequencies in 0.1 M KCl solution containing 1.0 mM K$_3$Fe(CN)$_6$; and (d) DPVs of 0.1 mM solution of the SY in 0.1 M PBS (pH = 7.5) at the GO, S–rGO, ZnS–SnS$_2$, and ZnS–SnS$_2$/S–rGO.

restricted diffusion process, while the semi-circular segment pertains to electron transfer throughout the reaction, with its diameter corresponding to the charge transfer resistance (R_{ct}). The resistance (R_{ct}) results from the faradaic interaction between the electrode and the electrolyte. The bare CPE, ZnS–SnS$_2$/CPE, and ZnS–SnS$_2$/S–rGO/CPE exhibited the R_{ct} values 6270 Ω, 15 900 Ω, and 1100 Ω, respectively. Furthermore, the ZnS–SnS$_2$/S–rGO/CPE demonstrated a very low R_{ct} value in comparison to the unmodified CPE and other modified CPEs, attributable to the integration of ZnS–SnS$_2$ nanostructures with S–rGO nanosheets, which facilitated the electron transfer process. The synergistic effects between ZnS–SnS$_2$ and S–rGO further improved the electrocatalytic efficacy of the ZnS–SnS$_2$/S–rGO nanocomposite. As a result, our suggested sensor material demonstrated low resistance, swift electron transit, improved conductivity, and advantageous catalytic activity. Moreover, the low resistance and high electrical conductivity of ZnS–SnS$_2$/S–rGO/CPE are expected to render it suitable for the development of an electrochemical sensor for the determination of SY.

3.3. Electrochemical behavior of SY on different electrodes

DPV is an effective method for examining the electrochemical characteristics of modified electrodes. Fig. 7d shows the DPV curves of 100 mM SY in 0.1 M PBS solution (pH = 7.5) on the surfaces of different electrodes. The response is extremely weak at the bare electrode's surface (bare CPE), but the modification of the carbon paste electrode's surface with the produced nanocomposite resulted in an enhanced intensity of the SY peak current. This increase in current can be seen as the increase in the number of active sites resulting from the placement of the sulfide compound between the S–rGO layers. Heterogeneous structures of the ZnS–SnS$_2$ sulfide compound used in electrode modification can facilitate the reaction kinetics and increase the electron transfer rate, although to increase the conductivity, a graphene compound is still required. In S–rGO by sulfur doping in the GO sheets, electrochemical activity and conductivity have increased, and increasing the distance between layers prevents re-accumulation of layers and disruption of electron transfer. Also, ZnS–SnS$_2$/S–rGO has a larger surface than the previous layers, providing sensor access and better electron transfer. Modifying the electrode with each alone cannot increase the oxidation current of SY, while the combination of the two as a composite significantly increases the intensity of the peak current because it covers other weaknesses and has a synergistic effect on each other. As a result, according to the explanations given and the results obtained from DPVs, it can be said that the modified electrode with ZnS–SnS$_2$/S–rGO compared to S–rGO or ZnS–SnS$_2$ is better than the rest of the electrodes and can be used as a sensor to detect SY.

3.4. Optimization of the experimental conditions

3.4.1. Optimization of the ratio of S–rGO to ZnS–SnS$_2$ for CPE modification. The ratio of S–rGO to ZnS–SnS$_2$ significantly affects CP modification. To examine this influence, the ratio was varied from 1:1, 1:1.5, and 1:2, to 1:3 during CP modification. Subsequently, DPVs were recorded in a 1 mM

[Fe(CN)$_6$]$^{3-/4-}$ solution in 0.1 M KCl, with the results presented in Fig. S3a (ESI†). As you can see, the best result was observed when the S–rGO to ZnS–SnS$_2$ ratio was 1:2. Consequently, it was employed as the ideal ratio in the CP modification.

3.4.2. Optimization of the kind of solvent for drop casting. To obtain the best performance, the solvent used for droplet application was investigated. For this purpose, 0.8 g of the intended modifier was dissolved in 2 ml of water, ethanol, Nafion, and DMF solvents, and then droplet application was performed to modify the electrode surface. Then DPVs were recorded in 1 mM [Fe(CN)$_6$]$^{3-/4-}$ in 0.1 M KCl solution, and you can see the obtained results in Fig. S3b (ESI†). Because the highest signal and the best performance were obtained in the presence of ethanol solvent, and no problems such as the falling of dried drops on the surface of the electrode were seen in the solution, it was used as the optimal solvent in the droplet application in the rest of the experiments.

3.4.3. Optimization of the amount of drop-casting. The quantity of modifiers in drop casting on the carbon paste electrode surface substantially influences the voltammetric results. Modified electrodes are recommended due to a weak signal at the unaltered electrode surface. Electrodes incorporating 30, 60, 80, and 90 μL modifiers were fabricated, followed by the recording of DPVs of 100 μM SY in 0.1 M PBS solution (pH = 7.5). The results are presented in Fig. S3c (ESI†). The modified electrode with 60 μL modifiers yielded the highest current, thus, it was designated as the optimal electrode and utilized in all subsequent tests.

3.5. Effect of pH

The DPV behaviors of SY in 0.1 M PBS with different pH values (5.0–8.5) were recorded and are shown in Fig. 8a. With the pH increasing, the oxidation peak potential (E_{pa}) shifted to more negative values, and the slope of E_{pa}–pH plot was about 35 mV pH^{-1}, indicating that the number of protons transferred in SY oxidation was not equal to the electrons (Fig. 8b). Because the highest SY signal was observed in pH = 7.5, it was used to determine SY.

3.6. Effect of scan rate

To investigate the effect of the scan rate on SY behavior, it was done as follows: first, a 100 μM SY in 0.1 M PBS solution (pH = 7.5) was prepared, and then it was taken at different scan rates of 10–100 mV s^{-1} from it on the surface of the ZnS–SnS$_2$/S–rGO/CPE, and the results are shown in Fig. 8c. As can be seen, by increasing the scan rate, the anodic peak current of SY increased and its oxidation potential shifted to more positive values, which is because there was not enough time for SY to reach the ZnS–SnS$_2$/S–rGO/CPE surface and carry out the oxidation process, and therefore, at high scan rates, a higher potential is needed for its oxidation. The results demonstrated that the peak current of SY oxidation displayed a linear correlation with the square root of the scan rate (Fig. 8d), confirming the diffusion-controlled process for the electro-oxidation reaction of SY.
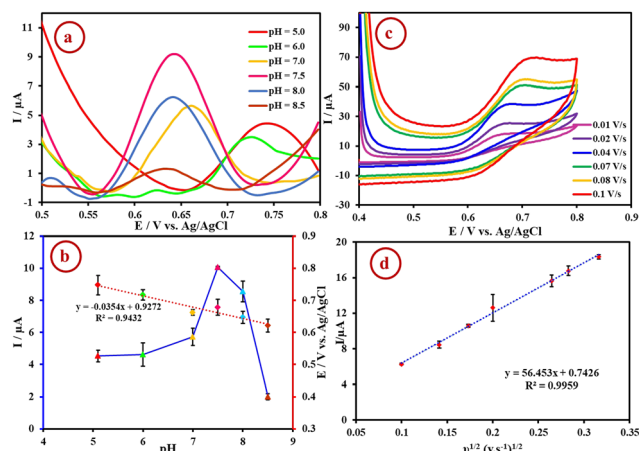
Fig. 8 (a) Cyclic voltammograms of 0.1 mM solutions of SY at the ZnS–SnS$_2$/S–rGO/CPE surface in 0.1 M PBS solution at different pH values (5.0 to 8.5) at a scan rate of 50 mV s^{-1}, (b) dependence of peak potential and peak current on pH; (c) CVs of 0.1 mM solutions of the SY at the ZnS–SnS$_2$/S–rGO/CPE surface in 0.1 M PBS solution (pH 7.5) at various scan rates, and (d) the corresponding plots are the square root of scan rate and the redox peak currents from the cyclic voltammograms.

3.7. Performance of the sensor

3.7.1. Calibration curve. Fig. 9a illustrates SY typical DPVs at the ZnS–SnS$_2$/S–rGO/CPE surface in optimum conditions. Increasing the SY concentration also increased the peak current. The variation in peak current establishes a strong correlation within the concentration range of 3–100 μM, shown by the regression equation I_p (μA) = 0.092C (μM) + 1.3665 (R^2 = 0.9913), with a detection limit of 140 nM (S/N = 3) (Fig. 9b). To compare this sensor's performance, we also contrasted its detection limit and linear dynamic range with those of the other sensors listed in Table 1. By comparing the results, it can be concluded that the fabricated sensor performs satisfactorily.
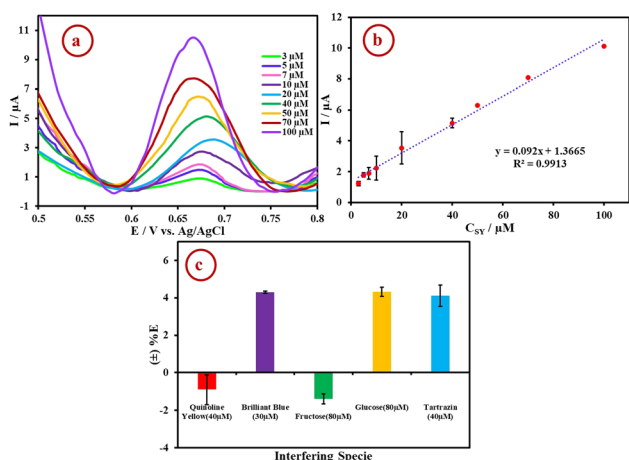

Fig. 9 (a) DPVs by increasing the concentration of SY from 3.0 μM to 100 μM in 0.1 M PBS solution (pH 7.5) at the ZnS–SnS$_2$/S–rGO/CPE surface; (b) the calibration curve; (c) effect of various interferents on the SY sensing response of ZnS–SnS$_2$/S–rGO/CPE. Error bars indicate the standard deviations of three repeated measurements.

3.7.2. Selectivity, reproducibility, and repeatability of the prepared sensors. One of the most important characteristics of a sensor is its selectivity and anti-interference. To study this character, three food dyes, including brilliant blue (30 μM), quinoline yellow (40 μM), and tartrazine (40 μM), and two species of glucose (80 μM) and fructose (80 μM) were used. DPVs were recorded by ZnS–SnS$_2$/S–rGO/CP electrodes in two different conditions: when the solution contained 40 μM of SY alone, and when the species mentioned above were also present at the specified quantities (Fig. 9c). All these species caused a shift in the peak SY current of less than ±5, indicating acceptable selectivity and anti-interference of the sensor.

Four distinct ZnS–SnS$_2$/S–rGO/CP electrodes were constructed to assess the sensor's reproducibility under identical circumstances. DPVs were obtained utilizing four electrodes, with a relative standard deviation (RSD) of 5.12%, signifying acceptable reproducibility.

For the repeatability test, one ZnS–SnS$_2$/S–rGO/CP electrode was prepared, and the 100 μM SY peak current was recorded after 1, 5, 10, and 15 min by the DPV method and the obtained RSD value of 2.41%, manifesting the acceptable repeatability of the sensor.

3.8. Real sample analysis

In the last stage of this research, to validate the practical application of the sensor designed for measuring SY developed by our research group, the sensor's results for various real food samples, including Fanta, orange-flavored jelly powder, and orange juice (utilizing the DPV method), were compared and

Table 1 Comparison of some characteristics of the ZnS–SnS$_2$/S–rGO/CPE sensor and previously reported sensors for electrochemical detection of SY

Electrode	Technique	Linear range (μM)	Detection limit (nM)	Ref.
Au/rGO/GCE	DPV	0.002–109.14	2	65
PLPA/GCE[a]	DPV	0.4–14.01	40	66
Poly(L-cysteine)/GCE	DPV	0.008–0.7	4	67
NiO/Ag/RGO/GCE	DPV	0.1–450	13	68
SiO$_2$@MIP PDA NPs/CPE[b]	DPV	0.0045–9.1	1.5	69
Cu@Cu$_2$O–BNPC/GCE[c]	DPV	0.01–8.0	2.4	70
MWCNT/GCE[d]	DPV	0.55–7.0	120	71
β-CD–PDDA–Gr/GCE[e]	DPV	0.05–20	12.5	72
ERGO/GCE[f]	DPV	0.05–1.0	19.2	73
Au–Pd/rGO/GCE	DPV	0.686–331.686	1.5	74
Chitosan–graphene/GCE	DPV	0.2–100.0	66.6	75
Gr/GCE[g]	LSV	1.0–100.0	300	76
CTAB-Gr/Pt/GCE[h]	DPV	0.08–10.0	4.2	77
ZnS–SnS$_2$/S–rGO	DPV	3.0–100.0	140	This work

[a] Poly(L-phenylalanine)/glassy carbon electrode. [b] Silica@molecularly imprinted polydopamine nanoparticles/carbon paste electrode. [c] Cu@Cu$_2$O nanoparticle-decorated B and N codoped porous carbon/glassy carbon electrode. [d] Multi-walled carbon nanotubes/glassy carbon electrode. [e] β-Cyclodextrin-coated poly(diallyldimethylammonium chloride)-functionalized graphene/glassy carbon electrode. [f] Electrochemically reduced oxide/glassy carbon electrode. [g] Graphene/glassy carbon electrode. [h] Hexadecyltrimethylammonium bromide–graphene/platinum/glassy carbon electrode.

Table 2 Determination of SY in real samples by the modified electrode and UV-vis ($n = 3$)

Sample	Added (µM)	Found by a modified electrode (µM) (%RSD)	Recovery (%)	Found by UV-vis (µM) (%RSD)	Recovery (%)
Orange-flavored jelly powder	—	15.67 (0.93)	—	15.18 (0.14)	
	10	24.41 (0.03)	95.09	25.86 (0.41)	102.70
	30	49.45 (3.85)	108.28	47.10 (0.18)	104.25
Orange juice	—	25.38 (6.56)	—	25.45 (0.05)	—
	10	35.98 (5.72)	101.70	36.06 (0.08)	101.72
	30	57.31 (1.69)	103.48	56.52 (0.01)	101.93
Fanta	—	15.55 (1.36)	—	16.10 (0.32)	—
	10	25.30 (0.75)	99.02	26.82 (0.40)	102.76
	30	46.00 (0.59)	100.99	47.28 (0.05)	102.56

analyzed against the UV-vis spectrophotometric method. The recovery rates ranged from 95.09% to 108.28%, confirming the sensor's efficacy for real food samples and indicating its potential for the development of portable electrochemical sensors for SY determination. The findings are summarized in Table 2.

4. Conclusion

In this work, the ZnS–SnS$_2$/S–rGO nanocomposite was first synthesized by chemical and hydrothermal methods and then characterized. After that, this nanocomposite was used to design a sensor for the selective determination and measurement of SY in real food samples. Under the optimal conditions, the detection limit and linear response range were obtained at 140 nM (S/N = 3) and 3–100 µM, respectively; then the selectivity, reproducibility, and repeatability were evaluated, and in general, the obtained results indicate the excellent performance of the sensor with acceptable accuracy and precision for the determination of SY.

Author contributions

Hanieh Ghaedi: conceptualization, methodology; Khadijeh Ghanbari: writing – review & editing, supervision, project administration, validation; Sepideh Bonyadi: writing – original draft.

Data availability

Data will be made available on request.

Conflicts of interest

The authors declare that they have no known competing financial interests or personal relationships that could have appeared to influence the work reported in this paper.

Acknowledgements

References

1 Y. Gao, T. Li, T. Zhang, M. Wang, L. Gao, Z. Yang and Z. Yang, *Food Chem.*, 2021, **365**, 130631.

2 A. T. Ezhil Vilian, S. M. Kang, S. Y. Oh, C. W. Oh, R. Umapathi, Y. S. Huh and Y. K. Han, *Food Chem.*, 2020, **323**, 126848.

3 P. A. Kolozof, A. B. Florou, K. Spyrou, J. Hrbac and M. I. Prodromidis, *Sens. Actuators, B*, 2020, **304**, 127268.

4 L. Xu, F. Yang, A. C. P. Dias and X. Zhang, *Food Chem.*, 2022, **385**, 132648.

5 P. M. Nowak, *J. Chromatogr. A*, 2020, **1620**, 460976.

6 R. Mirzajani and S. Karimi, *Ultrason. Sonochem.*, 2019, **50**, 239–250.

7 J. Shi, M. Huang, Q. Yang, Y. Xu, J. Wu, H. Liu, J. Zhang, F. Zheng and W. Dong, *Food Chem.*, 2025, **463**, 141133.

8 A. P. Nambiar, M. Sanyal and P. S. Shrivastav, *J. Chromatogr. A*, 2018, **1572**, 152–161.

9 M. Liu, Y. Fu, P. Jian, X. Zhou, Z. He, T. Gan, B. Wang, F. Jiang and C. Wu, *Sens. Actuators, B*, 2025, **427**, 137223.

10 E. Beyyavas and M. Aslanoglu, *Microchem. J.*, 2024, **199**, 110107.

11 G. E. Uwaya and K. Bisetty, *J. Electroanal. Chem.*, 2023, **951**, 117899.

12 Kh Ghanbari and F. Nejabati, *Anal. Methods*, 2020, **120**, 1650–1661.

13 A. A. Cardenas-Riojas, S. L. Calderon-Zavaleta, U. Quiroz-Aguinaga, G. Muedas-Taipe, S. M. Carhuayal-Alvarez, Y. F. Ascencio-Flores, M. Ponce-Vargas and A. M. Baena-Moncada, *ChemElectroChem*, 2024, **11**, e202300490.

14 A. A. Cardenas-Riojas, S. L. Calderon-Zavaleta, U. Quiroz-Aguinaga, E. O. López, M. Ponce-Vargas and A. M. Baena-Moncada, *J. Solid State Electrochem.*, 2023, **27**, 1969–1982.

15 X. Zhou, Z. Zhang, P. Yan, Y. Jiang, H. Wang and Y. Tang, *Mater. Chem. Phys.*, 2020, **244**, 122661.

16 L. Qie, W. Chen, X. Xiong, C. Hu, F. Zou, P. Hu and Y. Huang, *Adv. Sci.*, 2015, **2**, 1500195.

17 S. Sarr, N. F. Sylla, D. T. Bakhoum, N. M. Ndiaye, D. J. Tarimo, V. M. Maphiri, B. D. Ngom and N. Manyala, *J. Energy Storage*, 2022, **55**, 105666.

18 S. Hassanpoor and E. Tamri, *J. Alloys Compd.*, 2023, **932**, 167711.

19 D. Huang, L. Wang, Y. Zhan, L. Zou and B. Ye, *Biosens. Bioelectron.*, 2019, **140**, 111358.

20 T. T. Nguyet, C. M. Hung, H. S. Hong, N. X. Thai, P. V. Thang, C. T. Xuan, N. V. Duy, L. T. Theu, D. V. An, H. Nhuyen,

J. Z. Ou, N. D. Chien and N. D. Hoa, *Sens. Actuators, A*, 2024, **373**, 115384.

21 P. Li, C. Wang, Y. Wang, J. Chen, Y. Yang, C. Li, Y. Xie, P. Zhao and J. Fei, *Anal. Chim. Acta*, 2023, **1239**, 340681.

22 D. Meng, X. Zou, X. San, Y. Ji, Y. Zhang, G. Wang, J. Qi and Q. Jin, *Sens. Actuators, B*, 2024, **406**, 135359.

23 D. Kanakaraju and A. Chandrasekaran, *Sci. Total Environ.*, 2023, **868**, 161525.

24 Y. Ye, L. Wang, K. Liu and J. Li, *Microchem. J.*, 2020, **155**, 104749.

25 C. Wang, Y. Zhang, Y. Li, Y. Zhang, Y. Dong, D. Li and J. Zhang, *J. Alloys Compd.*, 2020, **820**, 153147.

26 J. Zhang, G. Huang, J. Zeng, Y. Shi, S. Lin, X. Chen, H. Wang, Z. Kong, J. Xi and Z. Ji, *J. Am. Ceram. Soc.*, 2019, **102**, 2810–2819.

27 X. Liu and J. Zhaeng, *Colloids Surf., A*, 2023, **656**(Part A), 130440.

28 F. P. D. Disouzaa, S. Ruspikaa, S.-M. Chena, R. Balajib, J. M. Devic, J.-Y. Penga and A. I. Jothi, *Microchem. J.*, 2023, **193**, 109087.

29 Y. Li, J. Zhang, S. Shang, F. Wang, H. Mei and H. Wu, *J. Alloys Compd.*, 2023, **965**, 171511.

30 X. Xu, S. Ma, X. Xu, S. Pei, T. Han and W. Liu, *J. Alloys Compd.*, 2021, **868**, 159286.

31 W. Yao, W. Zheng, J. Xu, C. Tian, K. Han, W. Sun and S. Xiao, *ACS Nano*, 2021, **15**, 7114–7130.

32 A. Shahmoradi, A. Hosseini, A. Akbarinejad and N. Alizadeh, *Anal. Chem.*, 2021, **93**, 6706–6714.

33 N. Yavari and Kh Ghanbari, *J. Mater. Chem. B*, 2025, **13**, 711–724.

34 J. Deng, G. Du, Y. Wang, H. Li, D. Han, S. Chen, Y. Wang, W. Zhao, S. Ding, Q. Su and B. Xu, *J. Alloys Compd.*, 2025, **1010**, 177172.

35 W. Zhang, L. Yang and S. Yin, *J. Colloid Interface Sci.*, 2024, **667**, 741–750.

36 S. Verma and B. Verma, *Int. J. Chem. Stud.*, 2018, **6**, 111–117.

37 X. Li, X. Xu, F. Xia, L. Bu, H. Qiu, M. Chen, L. Zhang and J. Gao, *Electrochim. Acta*, 2014, **130**, 305–313.

38 M. Nasrollahzadeh, F. Babaei, P. Fakhri and B. Jaleh, *RSC Adv.*, 2015, **5**, 10782–10789.

39 Y. Wang, M. Hu, D. Ai, H. Zhang, Z. H. Huang, R. Lv and F. Kang, *Nanomaterials*, 2019, **9**, 752–762.

40 Sh Hassanpoor and E. Tamri, *J. Alloys Compd.*, 2023, **932**, 167711.

41 S. P. Ega and P. Srinivasan, *J. Solid State Electrochem.*, 2021, **25**, 1–13.

42 A. Sadaqat, G. Ali, Z. Ali, F. J. Iftikhar and M. U. Hasan, *ACS Appl. Energy Mater.*, 2021, **4**, 13868–13877.

43 Kh Ghanbari and F. Nejabati, *J. Food. Meas. Charact.*, 2019, **13**, 1411–1422.

44 B. D. Ossonon and D. Bélanger, *RSC Adv.*, 2017, **7**, 27224.

45 J. Liu, Y.-G. Xu and L.-B. Kong, *Ionics*, 2021, **27**, 1781–1794.

46 Kh Ghanbari and A. Hajian, *J. Electroanal. Chem.*, 2017, **801**, 466–479.

47 K. Dai, J. Lv b, J. Zhang, C. Liang and G. Zhu, *J. Alloys Compd.*, 2019, **778**, 215–223.

48 T. Zhang, B. Yan, L. Zhang and X. Yang, *J. Alloys Compd.*, 2024, **990**, 174419.

49 J. Guo, W. Wang, Y. Li, J. Liang, Q. Zhu, J. Li and X. Wang, *RSC Adv.*, 2020, **10**, 26460.

50 Y. S. Yun, V.-D. Le, H. Kim, S.-J. Chang, S. J. Baek, S. Park, B. H. Kim, Y.-H. Kim, K. Kang and H.-J. Jin, *J. Power Sources*, 2014, **262**, 79–100.

51 S. Thakur, G. Das, P. K. Raul and N. Karak, *J. Phys. Chem. C*, 2013, **117**, 7636–7642.

52 G. Yang, X. Wan, Y. Su, X. Zeng and J. Tang, *J. Mater. Chem. A*, 2016, **4**, 12841–12849.

53 B. P. Vinayan, Z. Zhao-Karger, T. Diemant, V. S. K. Chakravadhanula, N. I. Schwarzburger, M. A. Cambaz, R. J. Behm, C. Kübel and M. Fichtner, *Nanoscale*, 2016, **8**, 3296–3306.

54 L. N. Liu, J. G. Dai, T. J. Zhao, S. Y. Guo, D. S. Hou, P. Zhang, J. Shang, S. Wang and S. Han, *RSC Adv.*, 2017, **7**, 35075.

55 A. Zhu, L. Oiao, Z. Jia, P. Tan, Y. Liu, Y. Ma and J. Pan, *Dalton Trans.*, 2017, **46**, 17032–17040.

56 A. C. Ferrari, J. C. Meyer, V. Scardaci, C. Casiraghi, M. Lazzeri, F. Mauri, S. Piscanec, D. Jiang, K. S. Novoselov, S. Roth and A. K. Geim, *Phys. Rev. Lett.*, 2006, **97**, 187401.

57 J. Ji, G. Zhang, H. Chen, S. Wang, G. Zhang, F. Zhang and X. Fan, *Chem. Sci.*, 2011, **2**, 484–487.

58 B. D. Ossonon and D. Belanger, *RSC Adv.*, 2017, **7**, 27224.

59 N. Karikalan, R. Karthik, S. M. Chen, C. Karuppiah and A. Elangovan, *Sci. Rep.*, 2017, **7**, 2494.

60 L. Chen, X. Cui, Y. Wang, M. Wang, R. Qiu, Z. Shu, L. Zhang, Z. Hua, F. Cui, C. Wei and J. Shi, *Dalton Trans.*, 2014, **43**, 3420–3423.

61 M. Favaro, F. Carraro, M. Cattelan, L. Colazzo, C. Durante, M. Sambi, A. Gennaro, S. Agnoli and G. Granozzi, *J. Mater. Chem. A*, 2015, **27**, 14334–14347.

62 C. Gurnani, S. L. Hawken, A. L. Hector, R. Huang, M. Jura, W. Levason, J. Perkins, G. Reid and G. B. G. Stenning, *Dalton Trans.*, 2018, **47**, 2628–2637.

63 Y. Qin, Z. Sun, W. Zhao, Z. Liu, D. Ni and Z. Ma, *Appl. Phys. A: Mater. Sci. Process.*, 2017, **123**, 355.

64 M. Mohebbi, Kh Ghanbari and F. Nejabati, *J. Electroanal. Chem.*, 2023, **946**, 117757.

65 J. Wang, B. Yang, H. Wang, P. Yang and Y. Du, *Anal. Chim. Acta*, 2015, **893**, 41–48.

66 M. Chao and X. Ma, *Food Anal. Methods*, 2014, **8**, 130–138.

67 K. Zhang, P. Luo, J. Wu, W. Wang and B. Ye, *Anal. Methods*, 2013, **5**, 5044–5050.

68 G. Lv, B. Shi, H. Huang, H. Chen, H. Feng, P. P. Zhou, W. Ye, Z. Zhang and Z. Yang, *J. Food Compos. Anal.*, 2021, **104**, 104136.

69 S. Bonyadi and Kh Ghanbari, *Microchem. J.*, 2021, **167**, 106322.

70 F. Yang, J. Wang, K. Yin and H. Pang, *ACS Omega*, 2022, **7**, 32068–32077.

71 P. Sierra-Rosales, C. Toledo-Neira and J. A. Squella, *Sens. Actuators, B*, 2017, **240**, 1257–1264.

72 X. Ye, Y. Du, D. Lu and C. Wang, *Anal. Chim. Acta*, 2013, **779**, 22–34.

73 Q. T. Tran, T. T. Phung, Q. T. Nguyen, T. G. Le and C. Lagrost, *Anal. Bioanal. Chem.*, 2019, **411**, 7539–7549.

74 J. Wang, B. Yang, K. Zhang, D. Bin, Y. Shiraishi, P. Yang and Y. Du, *J. Colloid Interface Sci.*, 2016, **481**, 229–235.

75 L. Magerusan, F. Pogacean, M. Coros, C. Socaci, S. Pruneanu, C. Leostean and I. O. Pana, *Electrochim. Acta*, 2018, **283**, 578–589.

76 F. Pogacean, M. Coros, V. Mirel, L. Magerusan, L. Barbu-Tudoran, A. Vulpoi, R. I. S. Staden and S. Pruneanu, *Microchem. J.*, 2019, **147**, 112–120.

77 L. Yu, M. Shi, X. Yue and L. Qu, *Sens. Actuators, B*, 2015, **209**, 1–8.